Highly Efficient and Stable FAPbI₃ Perovskite Solar Cells and Modules Based on Exposure of the (011) Facet

Kai Zhang[1,2], Bin Ding[2], Chenyue Wang[3], Pengju Shi[4], Xianfu Zhang[1,2], Cheng Liu[1], Yi Yang[1], Xingyu Gao[3], Rui Wang[4] ✉, Li Tao[5,6] ✉, Keith G. Brooks[2], Songyuan Dai[1], Paul J. Dyson[2] ✉, Mohammad Khaja Nazeeruddin[2] ✉, Yong Ding[1,2] ✉

HIGHLIGHTS

- The (011) facet has excellent charge transport properties achieving closer alignment of energy levels.

- By exploiting the (011) facet a device (0.06 cm²) and a module (29 cm²) achieved power conversion efficiencies of 25.24% and 21.12%, respectively.

ABSTRACT Perovskite crystal facets greatly impact the performance and stability of their corresponding photovoltaic devices. Compared to the (001) facet, the (011) facet yields better photoelectric properties, including higher conductivity and enhanced charge carrier mobility. Thus, achieving (011) facet-exposed films is a promising way to improve device performance. However, the growth of (011) facets is energetically unfavorable in FAPbI₃ perovskites due to the influence of methylammonium chloride additive. Here, 1-butyl-4-methylpyridinium chloride ([4MBP]Cl) was used to expose (011) facets. The [4MBP]⁺ cation selectively decreases the surface energy of the (011) facet enabling the growth of the (011) plane. The [4MBP]⁺ cation causes the perovskite nuclei to rotate by 45° such that (011) crystal facets stack along the out-of-plane direction. The (011) facet has excellent

charge transport properties and can achieve better-matched energy level alignment. In addition, [4MBP]Cl increases the activation energy barrier for ion migration, suppressing decomposition of the perovskite. As a result, a small-size device (0.06 cm²) and a module (29.0 cm²) based on exposure of the (011) facet achieved power conversion efficiencies of 25.24% and 21.12%, respectively.
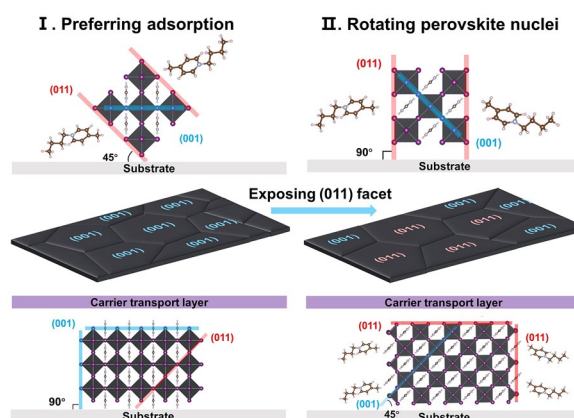
KEYWORDS Renewable energy; Perovskite solar cell; Perovskite solar module; Facet engineering

Kai Zhang, Bin Ding and Chenyue Wang contributed equally to this work.

✉ Rui Wang, wangrui@westlake.edu.cn; Li Tao, litao@hubu.edu.cn; Paul J. Dyson, paul.dyson@epfl.ch; Mohammad Khaja Nazeeruddin, mdkhaja.nazeeruddin@epfl.ch; Yong Ding, dingy@ncepu.edu.cn

1 Beijing Key Laboratory of Novel Thin-Film Solar Cells, North China Electric Power University, Beijing 102206, People's Republic of China
2 Institut des Sciences et Ingénierie Chimiques, Ecole Polytechnique Fédérale de Lausanne (EPFL), Lausanne 1015, Switzerland
3 Shanghai Synchrotron Radiation Facility (SSRF), Shanghai Advanced Research Institute, Chinese Academy of Sciences, Shanghai 201204, People's Republic of China
4 School of Engineering, Westlake University and Institute of Advanced Technology, Westlake Institute for Advanced Study, Hangzhou 310024, People's Republic of China
5 Hubei Yangtze Memory Laboratories, Wuhan 430205, People's Republic of China
6 School of Microelectronics, Hubei University, Wuhan 430062, People's Republic of China

1 Introduction

Perovskite solar cells (PSCs) have been studied extensively in the past decade, with a certified record power conversion efficiency (PCE) of 25.7% recently reported [1–3]. However, the PCE of perovskite solar modules (PSMs) decreases rapidly with increasing module size, and the efficiency of mini-modules (less than 200 cm^{-2}) is generally < 20% [4, 5]. Facets with different atomic arrangements and coordination impact the physicochemical properties of perovskites, such as carrier transport, surface energy level and stability [6–13]. Recently, the (111) facet in $FAPbI_3$ films has been demonstrated to improve the efficiency and stability of PSCs due to high carrier mobility, low exciton binding energies and thermodynamic stability [8, 9]. The perovskite single crystal provides a platform to investigate the photoelectric properties of different facets [6]. Devices fabricated on the (110) facet of $MAPbBr_3$ single crystals showed a 153% improvement of responsivity compared to those fabricated on the (100) and (110) facets of $MAPbI_3$ single crystals. Devices based on the (110) facet of $MAPbBr_3$ exhibited a lower dark current and enhanced photoresponse than other facets, which can be attributed to anisotropic arrangements and polarization differences [14, 15]. Therefore, it has been proposed that the (011) facet of $FAPbI_3$ should have excellent photoelectric performance, with the potential for enhancing the photovoltaic performance and stability of PSCs. However, a significant obstacle to exposing (011) facets in $FAPbI_3$ films is that the growth of the (011) plane is energetically unfavorable due to the influence of methylammonium chloride (MACl) additive [16–18]. Compared to the (011) plane of $FAPbI_3$, the (001) plane has a higher atom density, and MACl is more likely to incorporate into the (001) plane, reducing the surface energy of (001) planes more significantly than that of (011) planes. Controlled by thermodynamics, $FAPbI_3$ crystals grow along the (001) plane and the (011) facet disappears.

Dopant engineering is the most common strategy used to modulate facets of perovskite crystals [7–9, 19–21]. By using 3-(decyldimethylammonio)-propane-sulfonate as a dopant to change the growth rate of different facets of $MAPbI_3$, single crystals were tuned from (100) and (112) to (002) and (110), respectively [20]. Additionally, butylamine hydroiodide dopant triggered the transition of the $MA_3Bi_2I_9$ perovskite facet from (001) to (110) by decreasing the surface energy of the (011) facet [21]. Surface-anchoring alkylamine dopant was used to restrict the tilt of grains during growth, resulting in the formation of a (001) facet-dominant polycrystalline perovskite film. Based on this film, the device achieved a PCE of over 23% and demonstrated good operational stability [19]. Notably, a $FAPbI_3$ polycrystalline film assembled from single crystals with well-defined (001) and (111) facets was obtained using piperidine dopant [8, 9].

Here, we fabricated $FAPbI_3$ perovskite films doped with 1-butyl-4-methylpyridinium chloride ([4MBP]Cl), that results in the exposure of (011) facets, leading to improved charge carrier transport and energy level alignment. The [4MBP]Cl-doped perovskite films have fewer defects, suppressing non-radiative recombination. Photovoltaic devices and modules employing the perovskite with exposed the (011) facets exhibit outstanding PCEs and operational stability.

2 Experimental Sections

2.1 Materials

Formamidinium iodide (FAI) and phenethylammonium iodide (PEAI) were purchased from GreatCell. PbI_2 and 1-butyl-4-methylpyridinium chloride ([4MBP]Cl) were purchased from TCI. Spiro-OMeTAD, MACl and CsCl were obtained from Xi'an Polymer Light Technology. Isopropyl alcohol and acetone were purchased from Sinopharm Chemical Reagent Co., Ltd. Dimethylformamide (DMF), dimethyl sulfoxide (DMSO), chlorobenzene (CB), 4-tert-butylpyridine (tBP), bis(trifluoromethane)sulfonimide lithium salt (Li-TFSI) and FK209 Co(III) TFSI salt (Co-TFSI) were purchased from Sigma-Aldrich. Titanium tetrachloride ($TiCl_4$) and stannous chloride dehydrate ($SnCl_2 \cdot 2H_2O$) were purchased from Sinopharm Chemical Reagent Co., Ltd (China).

2.2 Small-size Device Fabrication

Small-size devices were fabricated using a planar architecture comprising FTO/compact TiO_2 layer (c-TiO_2)/ compact SnO_2 layer (c-SnO_2)/perovskite/Spiro-OMeTAD/ Au. The patterned FTO substrate (Asahi FTO glass, 12–13 Ω cm^{-2}) was sequentially cleaned with detergent (5% Hellmanex in water), deionized water, acetone and

isopropanol in an ultrasonic bath for 30 min. The c-TiO$_2$ and c-SnO$_2$ layers were prepared by chemical bath deposition (CBD) [22]. Then, the prepared FTO/c-TiO$_2$/c-SnO$_2$ substrates were transferred to a glove box for the deposition of the perovskite. The 1.4 M FAPbI$_3$ perovskite precursor (PbI$_2$:FAI = 1.05:0.95) was dissolved in DMF:DMSO = 7:3 (volume ratio) and 0.8 mol% MAPbBr$_3$, 5 mol% CsCl and 30 mol% MACl were added to the perovskite precursor solution. [4MBP]Cl was added at different molar ratios (0, 0.3, 0.5 and 0.7 mol%) to the perovskite solution. The perovskite precursor was spin-coated on the c-TiO$_2$/c-SnO$_2$ substrates with a two-step process. The first step was 1000 rpm for 10 s with an acceleration of 200 rpm s^{-1}. The second step was 5,000 rpm for 30 s with an acceleration of 1,000 rpm s^{-1}. 20 s into the second spinning step, 100 μL of CB anti-solvent was drop casted. The perovskite film was sequentially heated to 100 °C for 30 min and 150 °C for 10 min. For the post-treatment, 40 μL of PEAI in isopropanol (5 mg mL^{-1}) was deposited on the perovskite films at 5,000 rpm for 30 s, and 30 μL of Spiro-OMeTAD (90 mg mL^{-1} dissolved in CB) doped with tBP, Li-TFSI (520 mg mL^{-1} in acetonitrile), and Co-TFSI (300 mg mL^{-1} in acetonitrile) was deposited on top of the perovskite layer by spin-coating at 4000 rpm for 30 s. A ~70-nm gold electrode was then deposited on the films by thermal evaporation.

Fabrication of c-TiO$_2$ layer: The cleaned FTO substrate was placed in a sealed glass container and immersed in an aqueous TiCl$_4$ solution, prepared by mixing a 2-M aqueous TiCl$_4$ solution with deionized water in a 1:10 molar ratio. The 2-M aqueous TiCl$_4$ solution was prepared by dissolving TiCl$_4$ in deionized water at 0 °C. The glass container containing the FTO substrate was placed in a drying cabinet at 70 °C for 1 h. After cooling, the FTO/c-TiO$_2$ substrate was thoroughly rinsed with ethanol and deionized water, and then dried at 120 °C for 1 h.

Fabrication of c-SnO$_2$ layer: The FTO/c-TiO$_2$ substrate was placed in a sealed glass container and immersed in a solution consisting of 2 M-SnCl$_2$ in ethanol and deionized water, with a molar ratio of 1:50. The 2-M-SnCl$_2$ ethanol solution was prepared by dissolving SnCl$_2$·2H$_2$O in ethanol. Then, the glass container was placed in a drying cabinet at the temperature of 70 °C for 1 h. After cooling, the FTO/c-TiO$_2$/c-SnO$_2$ substrate was thoroughly rinsed with ethanol and deionized water, and subsequently annealed on a hot-plate at 190 °C for 1 h.

2.3 Module Fabrication

PSMs with 8 sub-cells connected in series were fabricated on FTO glass substrates with a size of 6.5 cm × 7.0 cm. The series interconnection of the module was realized by P1, P2 and P3 lines, which were patterned using a laser scribing system with 1064 nm of Nd:YAG/Nd:YVO4 lasers and a power of 20 W (Trotec). The FTO substrate was pre-patterned for P1 (with a width of 40 μm) by means of 60% laser power at a speed of 300 mm s^{-1} with a frequency of 65 kHz and pulse width of 120 ns. The subsequent processes for the preparation of c-TiO$_2$/c-SnO$_2$ substrates were the same as for the small-area devices as described above. The perovskite precursor deposition and fabrication procedures were also similar to those of the small-size solar cells except for the concentration of perovskite precursor. 1.3 M of perovskite precursor was employed to make the perovskite layer by spin-coating and the custom-made gas-induced pump method. The perovskite precursor was spin-coated on the c-TiO$_2$/c-SnO$_2$ substrates using a two-step process. The perovskite films were annealed at 100 ℃ for 1 h and 150 ℃ for 10 min. After cooling to room temperature, the procedures to spin-coat the PEAI passivation layer, and the spiro-OMeTAD layer were similar with those of the small-size devices. The P2 lines (with a width of 250 μm) were patterned before the Au evaporation process step with an average laser power of 15% at a speed of 1,000 mm s^{-1} and frequency of 65 kHz for pulse duration of 120 ns. A 70 nm-thick Au layer was then deposited, and the P3 line (with a width of 40 μm) was made using the same scribing condition as the P2 line. The distance between P1 and P3 was around 370 μm, and a geometric fill factor (GFF) was around 93.7%.

2.4 Characterization

The conductive atomic force microscope (C-AFM) was measured by Cypher ES Environmental AFM. UV–vis spectra are carried out on a UV–vis spectrophotometer (UV-3600 Plus, Shimadzu Co. Ltd, Japan). The current density–voltage (J-V) measurements were performed on a Keithley model 2400 digital source meter controlled by Test point software under a xenon lamp (450 W Xenon, AAA class). The light intensity was calibrated with a NREL-certified KG5-filtered Si reference diode. The active areas of small-size devices and modules were masked with a metal aperture of 0.06

and 29.0 cm^2 (the dead area was included). X-ray diffraction (XRD) patterns were obtained by an X-ray diffractometer (XRD, Smartlab SE, Rigaku, Japan) with Cu Kα radiation ($\lambda = 0.15406$ nm). PL mapping was carried out with a laser confocal Raman spectrometer (Princeton Instruments, Acton Standard Series SP-2558), a digital charge-coupled device (CCD) (PIXIS: 100B_eXcelon) and a 488-nm laser (PicoQuant LDH-P–C-485, 0.4 mW with a 1% optical density filter) using a homebuilt confocal microscope on a 20 µm×20 µm sample area.

2.5 Computational Methods

Density functional theory calculations used the Vienna Ab initio Simulation Package (VASP). The projected augmented wave (PAW) method and the Perdew–Burke–Ernzerhof (PBE) functional within the generalized gradient approximation (GGA) were employed to describe the interaction between ion-cores and valence electrons and exchange–correlation effects, and an energy cutoff of 500 eV was set for the plane-wave function expansion. The van der Waals (vdW) dispersion correction was described by the DFT-D3 correction. Transition states along the reaction pathway were determined using the nudged elastic band (NEB) method. The first Brillouin zone was sampled on a $3 \times 3 \times 1$ gamma (Γ)-centered k-space mesh for structural relaxation and static calculations. The atomic positions of all slabs were relaxed until the total energy changes were less than 1.0×10^{-5} eV and the maximum force relaxed down to 0.05 eV Å^{-1}. Calculations of transition states are based on the (001) perovskite surface.

The adsorption energy (E_{ads}) is defined as $E_{ads} = E_{[4MBP]^+/sur} - E_{[4MBP]^+} - E_{sur}$. $E_{[4MBP]^+/sur}$, $E_{[4MBP]^+}$ and E_{sur} are the energy of the [4MBP]$^+$ cation adsorbed on the perovskite surface, [4MBP]$^+$ and the perovskite surface, respectively.

3 Results and Discussion

3.1 Calculations and Model Analysis

In order to expose (011) facets, a dopant needs to selectively reduce the surface energy and growth rate of the (011) facet [20, 21]. As shown in Fig. 1a, the [4MBP]$^+$ cation was placed on the (001) and (011) facets of perovskite to

calculate the E_{ads}, respectively. The calculated E_{ads} showed that the [4MBP]$^+$ cation prefers to adsorb on the (011) facet because of $|E_{ads, (001)}| < |E_{ads, (011)}|$ (1.27 vs 2.14 eV). The selective adsorption of [4MBP]$^+$ lowers the surface energy of the (011) facet leading to slowing the growth of (011) plane due to the electrostatic interaction and steric hindrance provided by the [4MBP]$^+$ cation [20, 23, 24]. The calculations indicate that the preferential adsorption of [4MBP]Cl will change the orientation of perovskite nuclei. As illustrated in Fig. 1b, the interaction of [4MBP]$^+$ adsorbed on (011) facets should rotate perovskite nuclei by 45°. As a result, (011) crystal planes will stack along the out-of-plane direction, directly coming into contact with charge transport layers (Fig. S1), which is expected to accelerate charge carrier transport and collection [25, 26].

3.2 Crystallization Kinetics and Orientational Preference Studies

The role of chloride anions in enhancing carrier transport and stabilizing the perovskite structure has been extensively studied [17, 27]. To study the effect of the [4MBP]$^+$ cation on the crystallization kinetics of FAPbI$_3$ perovskite films, the films were doped with different concentrations of [4MBP]Cl (0–4 mol%). Perovskite films were analyzed using in situ grazing-incidence wide-angle X-ray scattering (GIWAXS). The GIWAXS intensity profiles of perovskites without [4MBP]Cl (control) and with [4MBP]Cl are plotted in Fig. 2a, b, respectively. For the [4MBP]Cl-doped film, the intensity of the (001) plane of FAPbI$_3$ at a q value of 10 nm^{-1} (where q was the scattering vector, $q = 4\pi \sin \theta/\lambda$) increases after 40 s, which is 20 s later than the control film, indicating that [4MBP]Cl retards the growth rate of FAPbI$_3$ perovskite. The slow growth of perovskite is beneficial in reducing defects and improving the quality of the film. Scanning electron microscopy (SEM) images reveal a significant increase in average grain sizes from ~ 0.6 to ~ 1.3 µm (Fig. S2). XRD measurements confirm that the (011) facet is exposed in the [4MBP]Cl-doped FAPbI$_3$ perovskite film (Fig. 2c). As the amount of [4MBP]Cl dopant increases, the diffraction intensity of the (001) facet continuously decreases, whereas the diffraction intensity of the (011) facet increases. Notably, the positions of the diffraction peak remain unchanged, presumably because the [4MBP]$^+$ cation is too large to
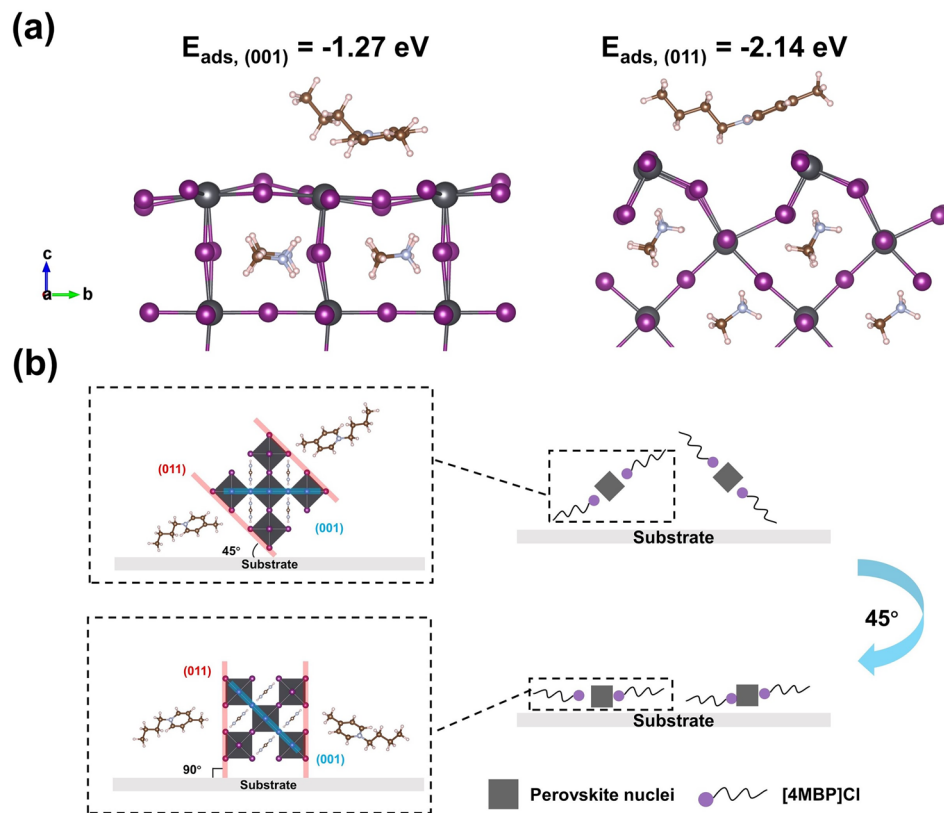
Fig. 1 Calculations and model analysis. **a** Calculated models of [4MBP]Cl adsorbed on (001) and (011) facets of FAPbI$_3$ and the corresponding adsorption energies. **b** Schematic of the proposed mechanism in which [4MBP]Cl changes the orientation of FAPbI$_3$ nuclei to expose the (011) facet

enter into the lattice. Time-of-flight secondary ion mass spectrometry (ToF–SIMS) was carried out in positive ion mode to determine the cross-sectional distribution of the [4MBP]$^+$ cation in PSCs. As illustrated in Fig. S3, the [4MBP]$^+$ cation is mainly located at the interface between the compact SnO$_2$ layer and the perovskite layer.

2D GIWAXS was used to probe the effect of the [4MBP]Cl dopant on the orientational preference of FAPbI$_3$ perovskite films. For the control perovskite film, the (001) plane showed the out-of-plane direction due to the presence of MACl (Fig. 2d) [16–18]. In contrast, the orientational preference for (001) planes in the [4MBP]Cl-doped perovskite films changed from the out-of-plane to ~45°-oriented direction. Simultaneously, the (011) planes preferentially orientate in the out-of-plane direction (Fig. 2e). According to the integrated GIWAXS intensity plot azimuthally along the ring at a q value approximate to 10 nm^{-1} (Fig. 2f), the azimuth of the (001) plane decreases from 90° to ~45° in the [4MBP]Cl-doped perovskite film. XRD was used to probe

the signal along the out-of-plane direction [28], which shows that the diffraction intensity of the (001) planes decrease as the [4MBP]Cl content increases (Fig. 2c).

3.3 Influence of the (011) Facets on Carrier Dynamics

Small-size devices were fabricated using a planar architecture comprising FTO/c-TiO$_2$/c-SnO$_2$/perovskite/spiro-OMeTAD/Au. The device with the best performance was obtained with the film containing 0.5 mol% [4MBP]Cl. Increasing the concentration of [4MBP]Cl enhances the (011) orientation, but it can also slow the crystal growth process and enlarge the grain size, leading to the formation of nonuniform and uncompact perovskite films with many pinholes, as shown in Fig. S4. These features ultimately lead to a decrease in device performance. Therefore, it is important to optimize the (011) preferential orientation and perovskite film quality. The statistical results of
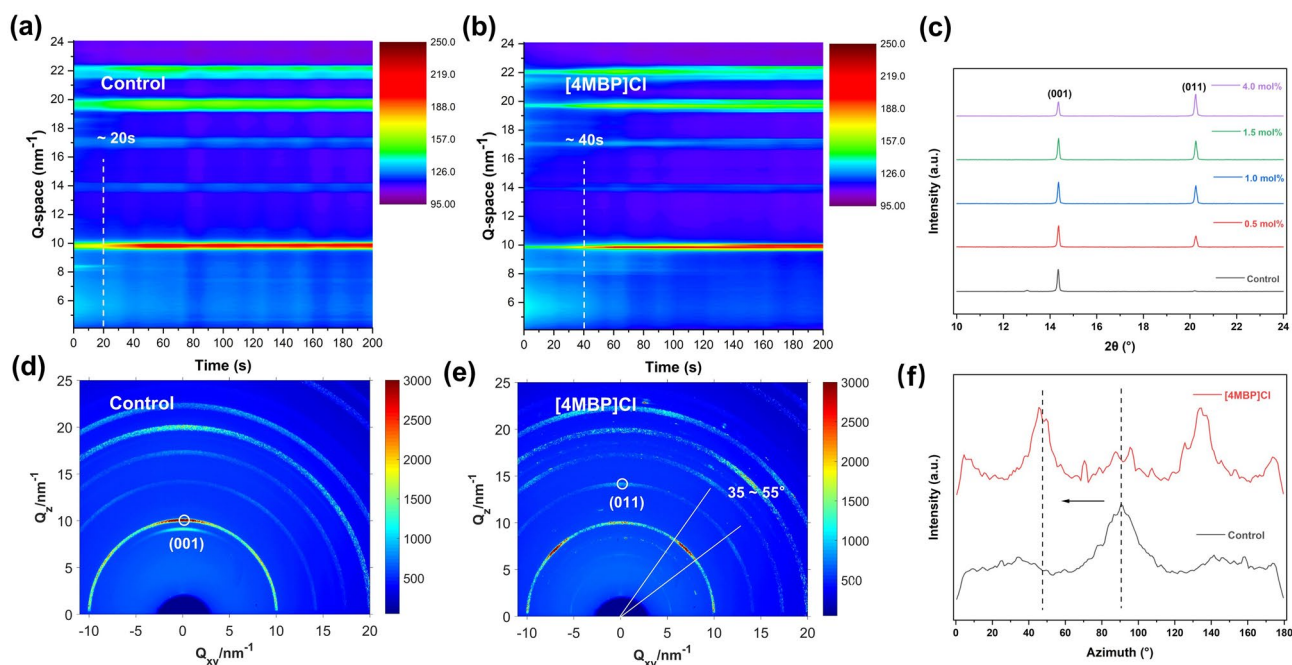
Fig. 2 Crystallization kinetics and orientational preference studies of the FAPbI$_3$ perovskite as a function of the [4MBP]Cl dopant. In-situ synchrotron radiation GIWAXS results of the FAPbI$_3$ perovskite films **a** without and **b** with 4 mol% [4MBP]Cl. **c** XRD patterns of perovskite films containing different concentrations of [4MBP]Cl (0–4 mol%). 2D GIWAXS patterns of the FAPbI$_3$ perovskite films **d** without and **e** with 4 mol% [4MBP]Cl. **f** Integrated GIWAXS intensity plots azimuthally along the ring at a q value approximate to 10 nm^{-1}, assigned to the (001) plane of perovskite films without and with 4 mol% [4MBP]Cl

small-size device's parameters, short-circuit current density (J_{sc}), open-circuit voltage (V_{oc}), PCE and fill factor (FF) were shown in Fig. S5. The average J_{sc} of all the devices are similar (range 26.20–26.27 mA cm^{-2}), which is consistent with the incident photon-to-current conversion efficiency (IPCE) results (Fig. S6). The devices with [4MBP]Cl-doped films have larger V_{oc} and FF values, which may be attributed to reduced defects and enhanced carrier transport. The champion device based on [4MBP]Cl-modified perovskite film achieved a J_{sc} of 26.29 mA cm^{-2}, a V_{oc} of 1.151 V, a FF of 83.4% and a PCE of 25.24%. In contrast, the performance of the control device comprises a J_{sc} of 26.28 mA cm^{-2}, a V_{oc} of 1.110 V, a FF of 83.1% and a PCE of 24.24% (Fig. S7). Further studies were therefore based on the perovskite film with the optimal [4MBP]Cl concentration of 0.5 mol% compared to the control device. The impact of the (011) facet on charge carrier dynamics was studied using conductive atomic force microscopy (C-AFM). Compared to the control film, the dark current is dramatically and uniformly enhanced in the [4MBP]Cl-modified perovskite film, with

the average dark current increasing from 45.2 to 55.4 pA (Fig. 3a, b). This enhancement may be attributed to the good electrical properties of (011) facets as reported previously [14, 15]. Additionally, the current at the grain boundaries is higher than at the grains, presumably due to ionic conduction at the grain boundaries [29].

As expected, since the perovskite lattice remains unchanged, exposing the (011) facets does not influence the optical energy band gap (E_g), confirmed by the UV–visible absorption spectra (Fig. S8). However, the (001) and (011) facets have different atomic arrangements, which causes a shift in the surface energy level of the perovskite. Ultraviolet photoelectron spectroscopy (UPS) was used to delineate the influence of the (011) facet on the surface energy level of perovskites (Fig. S9). The conduction band minimum (CBM) values decrease sharply from −4.12 to −4.33 eV following exposure of the (011) facets. As a result, the energy levels between the perovskite absorber and the electron transport layer (ETL) are better aligned, which facilitates electron extraction from the perovskite to the ETL (Fig. 3c). Energy level alignment is further confirmed by Kelvin probe force microscopy
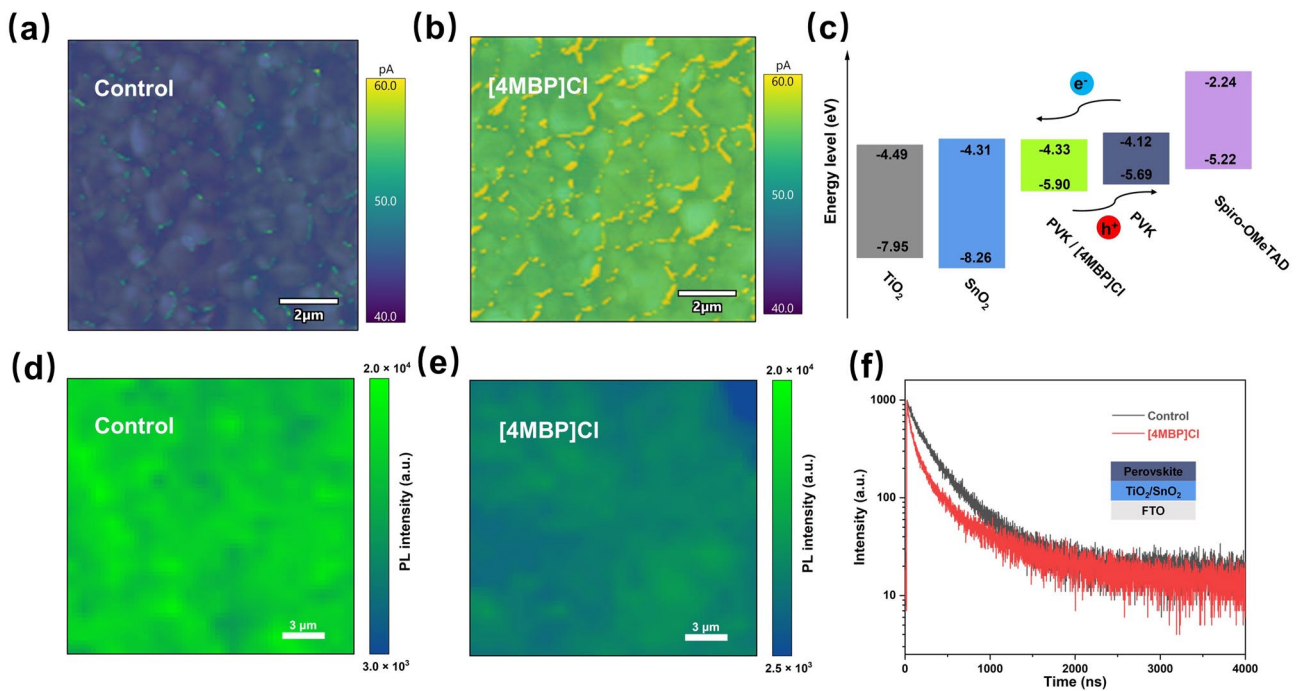
Fig. 3 The influence of the (011) facets on carrier dynamics. C-AFM current mapping images of the FAPbI$_3$ perovskite films **a** without and **b** with 0.5 mol% [4MBP]Cl. **c** Energy level diagram. PL mapping of the perovskite films **d** without and **e** with 0.5 mol% [4MBP]Cl deposited on FTO/ETL substrates. **f** TRPL spectra of the perovskite films without and with 0.5 mol% [4MBP]Cl deposited on FTO/ETL substrates

(KPFM). As shown in Fig. S10, the average contact potential difference (CPD) of grains in the control and [4MBP]Cl-modified perovskite film are 1.067 and 6.053 mV, respectively. Therefore, the (011) facet has a higher work function than the (001) facet in the perovskite films.

Steady-state photoluminescence (PL) mapping and time-resolved PL (TRPL) were used to further evaluate the effect of the (011) facets on charge carrier extraction and transport dynamics. The [4MBP]Cl-doped perovskite film deposited on FTO exhibited a higher PL intensity and a longer carrier lifetime than the control film, indicating the (011) facet inhibits non-radiative charge recombination (Fig. S11). The PL intensity of the [4MBP]Cl-modified perovskite film deposited on FTO/ETL is lower than that of the control perovskite film, demonstrating that the (011) facet promotes electron transfer from perovskite to ETL (Fig. 3d, e). As presented in Fig. 3f, compared with the control film, PL quenching of the [4MBP]Cl-doped film deposited on FTO/ETL is faster, indicative of a more efficient carrier extraction due to the better-matched energy level alignment.

A space-charge limited current (SCLC) model was used to characterize the density of trap states in the perovskite films. Dark current–voltage characteristics were collected on the electron-only devices (Fig. S12). The trap densities (N_t) were extracted using the equation: $N_t = \frac{2\varepsilon\varepsilon_0 V_{TFL}}{eL^2}$, where N_t denotes the trap state density, ε and ε_0 are the relative dielectric constant, and the vacuum dielectric constant respectively, V_{TFL} is the trap-filled limit voltage, e represents electron charge and L is the thickness of perovskite film [30]. V_{TFL} represents the bias voltage as the defects in the perovskite films were completely filled. Compared to the V_{TFL} value of the control film (0.203 V), the [4MBP] Cl-modified film has a smaller V_{TFL} value of 0.147 V. According to the equation, the trap densities decrease from 1.66×10^{15} to 1.43×10^{15} cm^{-3} in the [4MBP]Cl-doped film, attributed to the improved quality of the [4MBP]Cl-doped perovskite film. According to the equation, $V_{oc} = \frac{nkT\ln I}{q} + c$ from the Shockley–Read–Hall recombination mechanism (where T is the absolute temperature, k is the Boltzmann constant, q is the elementary charge, I is incident light intensity, c is the constant and n represents
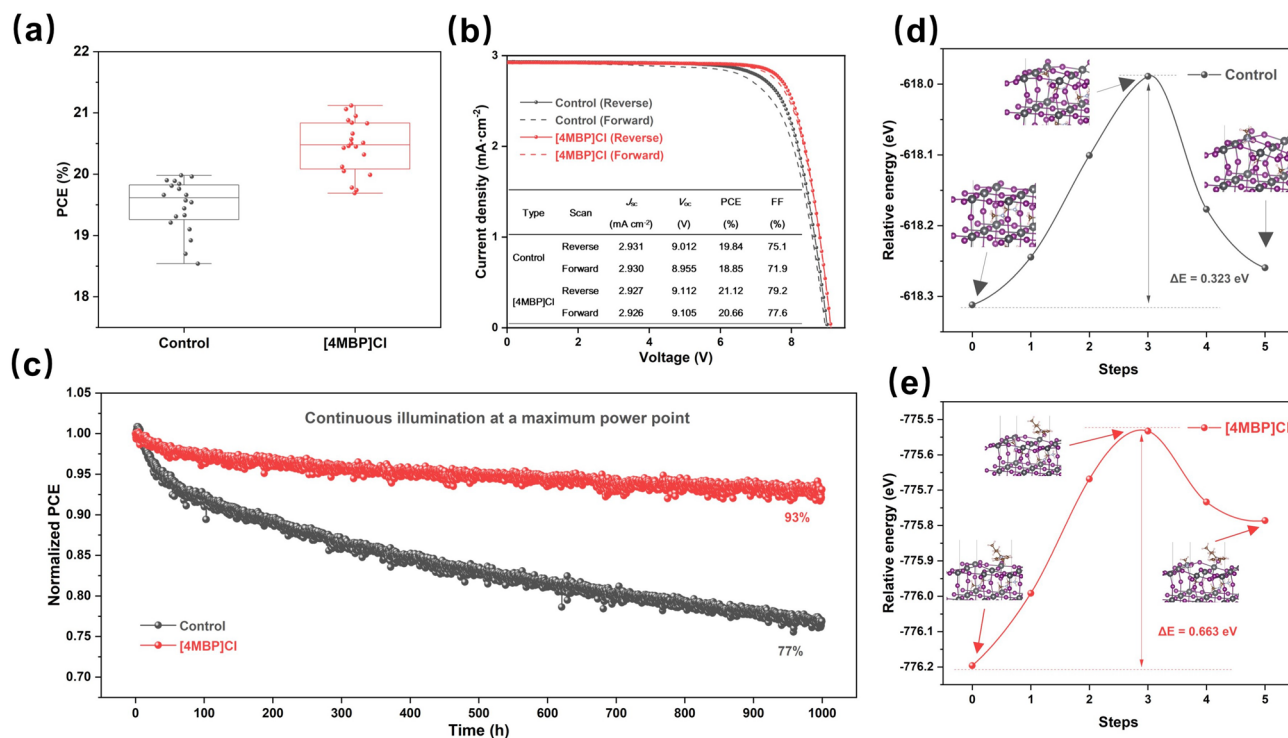
Fig. 4 Performance and stability of the photovoltaic devices and modules. **a** Corresponding PCE distribution of modules fabricated without and with 0.5 mol% [4MBP]Cl. **b** J-V curves of modules fabricated without and with 0.5 mol% [4MBP]Cl. **c** Operation stability of devices fabricated without and with 0.5 mol% [4MBP]Cl under continuous illumination at a maximum power point. Energy profiles of MA^+ ion migration in the perovskite **d** without and **e** with [4MBP]Cl. The structures of the NEB images at the initial, transition and final states are shown

an ideal factor), the closer the value of n to 1, the less trap-assisted non-radiational recombination exists in the device [31]. As presented in Fig. S13, the n value is 1.75 for the control device, decreasing to 1.39 in the [4MBP]Cl-modified device. Thus, non-radiative trap-dominated recombination is significantly suppressed due to the improved quality of perovskite films by [4MBP]Cl.

3.4 Performance and Stability of the Photovoltaic Devices and Modules

Based on the better performance of the [4MBP]Cl-doped devices, 6.5 cm × 7.0 cm modules were fabricated using the vacuum quenching-assisted method [32]. The aperture area of modules is 29.0 cm^2. Due to the improved carrier dynamics and perovskite film quality, the V_{oc} and FF of the [4MBP]Cl-doped modules are significantly enhanced compared to the control (Fig. S14). The average PCE increases from 19.50% for the control module to 20.45% for the [4MBP]Cl-doped module (Fig. 4a). The champion [4MBP]Cl-doped

module has a PCE of 21.12% with a J_{sc} of 2.927 mA cm^{-2}, a V_{oc} of 9.112 V and a FF of 79.2% in a reverse scan (RS), and a PCE of 20.66%, a J_{sc} of 2.926 mA cm^{-2}, a V_{oc} of 9.105 V and a FF of 77.6% in a forward scan (FS), for comparison with the champion control module see Fig. 4b. The hysteretic index (HI = (PCE$_{Reverse}$–PCE$_{Forward}$)/PCE$_{Reverse}$) decreases from 5.0% in the control module to 2.2% in the [4MBP]Cl-doped module, consistent with the reduced defects in the [4MBP]Cl-modified perovskite films.

The long-term operation stability was also studied by tracking the maximum power point under constant illumination (Fig. 4c). The [4MBP]Cl-doped device maintains 93% of its initial efficiency after 1,000 h, which compared favorably to the control device that retains only 77% of its initial efficiency. The increased photostability may be attributed to [4MBP]Cl located at grain boundaries, which could suppress ion migration and reduce defects.

The thermal stability of the PSCs was also probed with the unencapsulated devices and perovskite films heated at 60 °C under N_2 and in the dark. The control devices rapidly deteriorate to 78% of the original PCE after 480 h. In

contrast, the thermal stability of [4MBP]Cl-doped devices retains over 88% of the initial PCE after 864 h (Fig. S15). As shown in Fig. S15, the increased diffraction peak intensity of the control film at ca. 12.9° indicates that the perovskite decomposes to afford PbI_2 when maintained at 60 °C for 480 h. However, decomposition is suppressed in the [4MBP]Cl-doped perovskite films. DFT calculations using the NEB method were performed to model the MA^+ migration pathway and calculate the activation energy barrier (ΔE_a) for ion migration (Fig. 4d–e) [33]. The ΔE_a of the control and [4MBP]Cl-doped perovskite was estimated to be 0.323 and 0.663 eV, respectively, indicating the inhibited decomposition by the [4MBP]Cl. The higher ΔE_a may be attributed to the electrostatic interactions and steric hindrance induced by [4MBP]Cl on the perovskite surface, which suppresses the migration of MA^+ ions [24, 34].

4 Conclusions

Exposure of the (011) facet of the MACl-modified $FAPbI_3$ perovskite film using [4MBP]Cl has been shown to significantly enhance the charge transport ability of the perovskite film. The selective adsorption of the $[4MBP]^+$ cation on the (011) surface was found to decrease the surface energy of (011) surface and slow the growth of (011) plane during perovskite crystallization process. This interaction of the $[4MBP]^+$ cations also rotated the perovskite nuclei by 45°, leading to the (011) crystal planes stacking along the out-of-plane direction. Additionally, [4MBP]Cl greatly improved the stability of PSCs by reducing defects and increasing the activation energy barrier for the ion migration. The small-size device (0.06 cm^2) and module (29.0 cm^2) doped by the (011) facet achieved champion efficiencies of 25.24 and 21.12%, respectively. The [4MBP]Cl-doped device demonstrated good operational and thermal stability, indicating that this strategy could lead to more efficient and stable perovskite solar cells in future.

Declaration

Competing of Interest The authors declare no interest conflict. They have no known competing financial interests or personal relationships that could have appeared to influence the work reported in this paper.

Supplementary Information The online version contains supplementary material available at https://doi.org/10.1007/s40820-023-01103-8.

References

1. J. Park, J. Kim, H.S. Yun, M.J. Paik, E. Noh et al., Controlled growth of perovskite layers with volatile alkylammonium chlorides. Nature (2023). https://doi.org/10.1038/s41586-023-05825-y
2. J.Y. Kim, J.W. Lee, H.S. Jung, H. Shin, N.G. Park, High-efficiency perovskite solar cells. Chem. Rev. **120**(15), 7867–7918 (2020). https://doi.org/10.1021/acs.chemrev.0c00107
3. L. Zhang, X. Pan, L. Liu, L. Ding, Star perovskite materials. J. Semicond. **43**(3), 030203 (2022). https://doi.org/10.1088/1674-4926/43/3/030203
4. X. Luo, X. Lin, F. Gao, Y. Zhao, X. Li et al., Recent progress in perovskite solar cells: From device to commercialization. Sci. China Chem. **65**(12), 2369–2416 (2022). https://doi.org/10.1007/s11426-022-1426-x
5. H. Wang, Z. Qin, Y. Miao, Y. Zhao, Recent progress in large-area perovskite photovoltaic modules. Trans. Tianjin Univ. **28**(5), 323–340 (2022). https://doi.org/10.1007/s12209-022-00341-y
6. A. Capitaine, B. Sciacca, Monocrystalline methylammonium lead halide perovskite materials for photovoltaics. Adv. Mater. **33**(52), e2102588 (2021). https://doi.org/10.1002/adma.202102588

7. Z. Fang, N. Yan, S. Liu, Modulating preferred crystal orientation for efficient and stable perovskite solar cells-from progress to perspectives. InfoMat **4**(10), e12369 (2022). https://doi.org/10.1002/inf2.12369

8. C. Ma, M. Grätzel, N.-G. Park, Facet engineering for stable, efficient perovskite solar cells. ACS Energy Lett. **7**(9), 3120–3128 (2022). https://doi.org/10.1021/acsenergylett.2c01623

9. C. Ma, M.-C. Kang, S.-H. Lee, S.J. Kwon, H.-W. Cha et al., Photovoltaically top-performing perovskite crystal facets. Joule **6**(11), 2626–2643 (2022). https://doi.org/10.1016/j.joule.2022.09.012

10. C. Ma, F.T. Eickemeyer, S.H. Lee, D.H. Kang, S.J. Kwon, M. Grätzel, N.G. Park, Unveiling facet-dependent degradation and facet engineering for stable perovskite solar cells. Science **379**(6628), 173–178 (2023). https://doi.org/10.1126/science.adf3349

11. W. Zhu, Q. Wang, W. Chai, D. Chen, D. Chen et al., Tailored interfacial crystal facets for efficient $CH_3NH_3PbI_3$ perovskite solar cells. Org. Electron. **78**, 105598 (2020). https://doi.org/10.1016/j.orgel.2019.105598

12. H. Dong, L. Zhang, W. Zhang, J. Wang, X. Zhang et al., Single crystals of perovskites. J. Semicond. **43**(12), 120201 (2022). https://doi.org/10.1088/1674-4926/43/12/120201

13. Y. Li, L. Ding, Single-crystal perovskite devices. Sci. Bull. **66**(3), 214–218 (2021). https://doi.org/10.1016/j.scib.2020.09.026

14. Z. Zuo, J. Ding, Y. Zhao, S. Du, Y. Li et al., Enhanced optoelectronic performance on the (110) lattice plane of an $MAPbBr_3$ single crystal. J. Phys. Chem. Lett. **8**(3), 684–689 (2017). https://doi.org/10.1021/acs.jpclett.6b02812

15. J. Ding, L. Jing, Y. Yuan, J. Zhang, Q. Yao et al., Low defect density and anisotropic charge transport enhanced photoresponse in pseudo-cubic morphology of $MAPbI_3$ single crystals. ACS Appl. Energy Mater. **3**(11), 10525–10532 (2020). https://doi.org/10.1021/acsaem.0c01565

16. Z. Xu, Z. Liu, N. Li, G. Tang, G. Zheng et al., A thermodynamically favored crystal orientation in mixed formamidinium/methylammonium perovskite for efficient solar cells. Adv. Mater. **31**(24), e1900390 (2019). https://doi.org/10.1002/adma.201900390

17. M. Kim, G.-H. Kim, T.K. Lee, I.W. Choi, H.W. Choi et al., Methylammonium chloride induces intermediate phase stabilization for efficient perovskite solar cells. Joule **3**(9), 2179–2192 (2019). https://doi.org/10.1016/j.joule.2019.06.014

18. F. Ye, J. Ma, C. Chen, H. Wang, Y. Xu et al., Roles of MACl in sequentially deposited Bromine-free perovskite absorbers for efficient solar cells. Adv. Mater. **33**(3), e2007126 (2021). https://doi.org/10.1002/adma.202007126

19. X. Zheng, Y. Hou, C. Bao, J. Yin, F. Yuan et al., Managing grains and interfaces via ligand anchoring enables 22.3%-efficiency inverted perovskite solar cells. Nat. Energy **5**(2), 131–140 (2020). https://doi.org/10.1038/s41560-019-0538-4

20. Y. Liu, X. Zheng, Y. Fang, Y. Zhou, Z. Ni et al., Ligand assisted growth of perovskite single crystals with low defect density. Nat. Commun. **12**(1), 1686 (2021). https://doi.org/10.1038/s41467-021-21934-6

21. W. Wang, M. Cai, G. Wu, L. Zhu, X. Liu et al., Facet control of the lead-free methylammonium bismuth iodide perovskite single crystals via ligand-mediated strategy. Cryst. Growth Des. **21**(10), 5840–5847 (2021). https://doi.org/10.1021/acs.cgd.1c00721

22. B. Ding, S.-Y. Huang, Q.-Q. Chu, Y. Li, C.-X. Li et al., Low-temperature SnO_2-modified TiO_2 yields record efficiency for normal planar perovskite solar modules. J. Mater. Chem. A **6**(22), 10233–10242 (2018). https://doi.org/10.1039/c8ta01192c

23. C. Liu, Y. Yang, K. Rakstys, A. Mahata, M. Franckevicius et al., Tuning structural isomers of phenylenediammonium to afford efficient and stable perovskite solar cells and modules. Nat. Commun. **12**(1), 6394 (2021). https://doi.org/10.1038/s41467-021-26754-2

24. J. Yang, W. Sheng, R. Li, L. Gong, Y. Li et al., Uncovering the mechanism of poly(ionic-liquid)s multiple inhibition of ion migration for efficient and stable perovskite solar cells. Adv. Energy Mater. **12**(15), 2103652 (2022). https://doi.org/10.1002/aenm.202103652

25. G. Zheng, C. Zhu, J. Ma, X. Zhang, G. Tang et al., Manipulation of facet orientation in hybrid perovskite polycrystalline films by cation cascade. Nat. Commun. **9**(1), 2793 (2018). https://doi.org/10.1038/s41467-018-05076-w

26. Z. Wang, Q. Lin, F.P. Chmiel, N. Sakai, L.M. Herz et al., Efficient ambient-air-stable solar cells with 2D–3D heterostructured butylammonium-caesium-formamidinium lead halide perovskites. Nat. Energy **2**(9), 17135 (2017). https://doi.org/10.1038/nenergy.2017.135

27. M.I. Saidaminov, J. Kim, A. Jain, R. Quintero-Bermudez, H. Tan et al., Suppression of atomic vacancies via incorporation of isovalent small ions to increase the stability of halide perovskite solar cells in ambient air. Nat. Energy **3**(8), 648–654 (2018). https://doi.org/10.1038/s41560-018-0192-2

28. M. Qin, P.F. Chan, X. Lu, A systematic review of metal halide perovskite crystallization and film formation mechanism unveiled by in situ GIWAXS. Adv. Mater. **33**(51), e2105290 (2021). https://doi.org/10.1002/adma.202105290

29. D. Seol, A. Jeong, M.H. Han, S. Seo, T.S. Yoo et al., Origin of hysteresis in $CH_3NH_3PbI_3$ perovskite thin films. Adv. Funct. Mater. **27**(37), 1701924 (2017). https://doi.org/10.1002/adfm.201701924

30. Y. Zhao, P. Zhu, S. Huang, S. Tan, M. Wang et al., Molecular interaction regulates the performance and longevity of defect passivation for metal halide perovskite solar cells. J. Am. Chem. Soc. **142**(47), 20071–20079 (2020). https://doi.org/10.1021/jacs.0c09560

31. Z. Wenyu, L. Xiaojie, H. Benlin, G. Zekun, Z. Jingwei et al., Interface engineering of imidazolium ionic liquids toward efficient and stable $CsPbBr_3$ perovskite solar cells. ACS Appl. Mater. Interfaces **12**(4), 4540–4548 (2020). https://doi.org/10.1021/acsami.9b20831

32. Y. Ding, B. Ding, H. Kanda, O.J. Usiobo, T. Gallet et al., Single-crystalline TiO_2 nanoparticles for stable and efficient

perovskite modules. Nat. Nanotechnol. **17**(6), 598–605 (2022). https://doi.org/10.1038/s41565-022-01108-1

33. J. Haruyama, K. Sodeyama, L. Han, Y. Tateyama, First-principles study of ion diffusion in perovskite solar cell sensitizers. J. Am. Chem. Soc. **137**(32), 10048–10051 (2015). https://doi.org/10.1021/jacs.5b03615

34. R. Xia, Z. Fei, N. Drigo, F.D. Bobbink, Z. Huang et al., Retarding thermal degradation in hybrid perovskites by ionic liquid additives. Adv. Funct. Mater. **29**(22), 1902021 (2019). https://doi.org/10.1002/adfm.201902021